Journal of Power Sources 500 (2021) 229918

Contents lists available at ScienceDirect

Journal of Power Sources

journal homepage: www.elsevier.com/locate/jpowsour

Improving stability using a mixed ion/hybrid electrolyte strategy in a sodium ion capacitor

Bala Krishnan Ganesan [a], Ranjith Thangavel [b,c], Megala Moorthy [a], Seo - Jun Lee [a], Won-Sub Yoon [b], Yun-Sung Lee [a,*]

[a] School of Chemical Engineering, Chonnam National University, Gwangju, 61186, South Korea
[b] Department of Energy Science, Sungkyunkwan University, Suwon, 16419, South Korea
[c] The Institute of New Paradigm of Energy Science Convergence, Sungkyunkwan University, Suwon, 16419, Republic of Korea

HIGHLIGHTS

- Sodium ion vs Mixed ion hybrid capacitor.
- Stability more than two-fold (40000 cycles).
- XPS and electron probe micro analysis (EPMA) mapping to unravel mechanism.
- Schematic of S dissolution in presence of Na ion and mixed ion/hybrid.

GRAPHICAL ABSTRACT

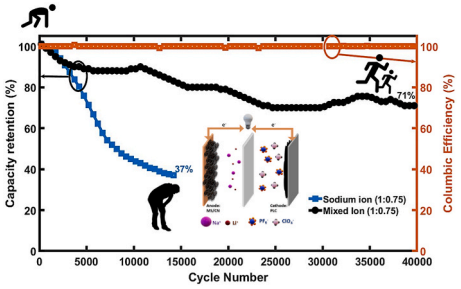

ARTICLE INFO

Keywords:
Na ion capacitor
Mixed ion electrolyte
MoS_2 anode
Sulfur dissolution
Electron probe microanalysis (EPMA)

ABSTRACT

In Sodium-ion capacitors (SICs), employing high-capacity anodes based on alloying/conversion reactions can potentially alleviate the performance issues but are susceptible to rapid capacity fading due to consistent dissolution of the electrode surface by the electrolyte. Herein, we extend the "hybrid mixed electrolyte" strategy to ion capacitors for overcoming the rapid cycle decay issues in high-energy SICs: molybdenum disulphide (MoS_2, MS) nanocrystals grown on carbon nitride (C_3N_4, CN), denoted as MS/CN, as anode exhibited remarkable performance in both sodium electrolyte and replaced with a hybrid mixed electrolyte comprising larger Na^+ ions and smaller Li^+ ions. Thus, constructed SICs exhibited a high energy density of 124 Wh Kg^{-1} with a mixed ion electrolyte, and low energy loss (71% retention after 40000 cycles) with a hybrid electrolyte (lower than conventional sodium-ion-based electrolyte: 37% retention after 15000 cycles). Systematic investigations, including X-ray photoelectron spectroscopy and electron probe microanalysis, revealed an advantageous formation of a stable interface for electrode and electrolyte.

1. Introduction

Energy has become one of the most highly demanded commodities in recent decades, and various types of energy storage devices have been developed to accommodate these demands. Batteries and supercapacitors are two primary examples of highly commercialized and

* Corresponding author.
E-mail address: leeys@chonnam.ac.kr (Y.-S. Lee).

https://doi.org/10.1016/j.jpowsour.2021.229918
Received 17 January 2021; Received in revised form 18 March 2021; Accepted 10 April 2021
Available online 8 May 2021

widely used electrochemical energy storage devices with numerous applications. Batteries can store significant amounts of energy via intercalation chemistry [1,2], a process which, however, requires considerable amounts of time. Conversely, capacitors can store analogous amounts of electrical energy in exponentially less time. Energy sources such as solar, hydro, and even fuel cells are capable of producing enormous amounts of energy; nevertheless, devices capable of instantaneously storing such energy are required. The same applies for electric vehicles requiring additional energy for longer mileage, which could benefit from shorter refilling/recharging times. Hence, a new class of storage devices with high energy output at increased power conditions is necessary. Hybrid ion capacitors (HCs) bridge the performance gap between batteries and supercapacitors by combining the features of both systems. The high-energy/high-power behavior of HCs stems from two main charge–storage mechanisms involved during the storage process: the insertion/extraction mechanism on the battery-type anode and the simultaneous anion adsorption/desorption mechanism on the cathode.

Sodium-ion capacitors (SICs) emerged as an advantageous device owing to the wide availability of sodium and their superior performance compared with their lithium counterparts. In SICs, intercalation-type electrodes such as $Na_3V_2(PO_4)_3$ (NVP), $NaTi_2(PO_4)_3$ (NTP), and $Na_3(VO)_2(PO_4)_2F$ (NVOPF), commonly referred to as Sodium (Na) Super Ionic CONductors (NASICONs), are utilized as the anode, and porous activated carbon is utilized as the cathode. Commonly, NASICON-type insertion electrodes have been synthesized in various forms, such as carbon encapsulated [3–5], graphene composites [6,7], and nanocages [8], further, other microstructures have also been adopted [9–12]. Although SICs employing intercalation anodes have achieved power performances comparable with those of supercapacitors, there is still significant room for improvement. The poor energy densities in SICs are mainly attributed to the low capacities of intercalation anodes and their high redox potentials.

Replacing the low-capacity intercalation anodes with high-capacity alloy-type anodes could mitigate energy limitations and power capabilities in conventional electrodes. Few notable high-capacity alloy anodes based on titanium [13], tungsten [14–17], tin [18,19], and cobalt [20,21] have exhibited an energy density of 110–150 Wh Kg^{-1} when employed in SICs. Despite the advantages, high-capacity alloy-type anodes presented a limited scope for use in SICs; this is because of the rapid capacity loss with cycling, severe polarization from irreversibility, and significant volume variation issues. The abnormal volume changes during the alloying/dealloying reactions severely affected stability and the energy output at higher power densities. A combination of several different approaches is required for overcoming the inherent issues in SICs when an alloy-type anode is used as a Na-ion host. An effective architecture, in conjunction with a suitable ion/electron transport channel in alloy-type anodes, can greatly improve the kinetics of Na-ion storage reactions.

Among several alloy-based anodes, dichalcogenides have been extensively studied in recent years because of their graphite-like layered formation during synthesis, which facilitates ion diffusion (generated from the presence of sulfur carrying multiple Li^+ and Na^+ active ions). The constructive properties of dichalcogenides render them advantageous candidates for obtaining high-performance hybrid capacitors. For instance, Zeng et al. [15] developed a hierarchical nanocomposite, based on tungsten disulfide (WS_2), which exhibited superior capacity and stability. This impressive performance was attributed to its hierarchical structure, which is also observed in other chalcogens, such as tin disulfide (SnS_2), studied by Thangavel et al. and Zhang et al. [22,23]. Similarly, Mitlin et al. [24,25], among other researchers [26–28], have extensively researched the advantageous characteristics of MoS_2 (e.g., storage performance, cyclic stability, flexibility etc.), enabling the synthesis of desired architectures such as nanoflowers [29] and nano sheets [30–32], which facilitate the achievement of its theoretical capacity (~670 mAh/g) [33]; however, its intrinsic poor conductivity and acute structural degradation during the charge–discharge process severely impact its capacity after a few (~1000) cycles.

To achieve high-kinetics reactions, a MoS_2 anode with a hierarchical, highly porous structure that can easily accommodate Na^+ ions is essential; therefore, its specific surface area becomes a highly relevant property (which is higher for nanostructures, compared with microstructures). Hence, MoS_2 possessing a nanocrystal morphology, larger interlayer distance, and higher immunity to microcrystal-related complications (such as distortion, defects, and cracking) can be beneficial. On the other hand, combining MoS_2 with 2D carbon could potentially improve the conductivity of a 2D sodium host [23,34]. In this regard, C_3N_4 is a composite material exhibiting natural pores, a graphitic sheet structure, and enhanced conductivity that can benefit the diffusion kinetics of a hybrid capacitor (by increasing ion diffusivity due to its porous carbon structure), which in turn will increase the power density.

Nonetheless, the lifecycle issue in alloy-based anodes needs to be addressed, and this requires a new approach to stabilize the Na-ion host interface. Dichalcogenides (MoS_2) exhibit a rapid capacity decay and energy loss when employed in energy storage applications, mainly due to the dissolution of sulfur, which acts as an active site for alloying. Herein, we adopted a novel "mixed-ion hybrid electrolyte" strategy to overcome the capacity loss issue. The drawback of current Na^+ ion systems is the larger ionic size of sodium compared with that of lithium; hence, Na^+ ions require larger interlayer distances to be accommodated in a host material [27]. The space is not completely utilized even in larger interlayered structures, owing to the bulkier Na ions bottlenecking the diffusion pathways; therefore, instead of altering the host electrodes, selecting ions with suitable sizes is a more facile approach. In our proposed strategy, a theoretical increase in maximum capacity can be achieved by mixing equal proportions of Li and Na ions, considering that larger ions occupy larger spaces whereas smaller ions can be accommodated in smaller gaps and voids. Consequently, additional capacity is induced by optimally exploiting the entirety of the charge storage space in SICs, as well as by reducing Li electrolytes in Li-ion capacitors. Given the abundance of sodium and increased performance of Li, the mixed-ion strategy synergistically balances the rival ions. When Li ions are introduced in a Na-based system, apart from enhancing performance, the damage caused by Na ions is mitigated. Zhu et al. [35] demonstrated the improvements in terms of stability and performance in a Na-ion based MoS_2/C dual-ion battery. The same strategy was followed for improving capacity and performance in various batteries based on electrodes such as NVPF [36,37] and NVP [38,39]. Despite the frequent employment of this strategy, the factors inducing the stability improvements have not been thoroughly investigated. Several researchers are currently studying the mixed/dual-ion strategy for extracting additional capacity, as well improving stability, by altering numerous parameters (including the secondary electron image) [40,41]. For this purpose, comprehending the mechanisms of the synergistic effects via relevant characterization techniques and simultaneous experimental demonstration is of eminent importance.

Herein, we confirmed that an alloy-type anode (MoS_2), in conjunction with a new class of hybrid electrolyte ($NaClO_4$+$LiPF_6$), can deliver high energy outputs in SICs, while exhibiting superior stability. By merging MoS_2 nanocrystals with a C_3N_4 backbone in a new hybrid electrolyte, we achieved a remarkable energy density of 112 Wh Kg^{-1} without compromising stability up to 40000 cycles. Replacing conventional sodium-ion electrolytes with hybrid mixed electrolytes can enhance both energy density and cyclic stability. As such, the findings of this study provide insights for developing ultra-high energy SICs with superior stability.

2. Materials and methods

2.1. Synthesis of MoS_2/C_3N_4 (MS/CN) system

High-interlayer-distance MoS_2 was synthesized using a straightforward one-step solvothermal process [27,42], summarized as follows:

0.3 mol of ammonium molybdate tetrahydrate (Alfa Aesar, 99% purity) was mixed thoroughly with 0.6 mol of thioacetamide (TAA, Sigma-Aldrich, 98% purity); both substances were used untreated. Subsequently, 25 wt% of C_3N_4 was added to procure the corresponding supported system. The resulting mixture was poured into a tightly sealed Teflon-lined autoclave chamber and was hydrothermally processed at 160 °C for 24 h. The obtained precipitate was centrifuged, followed by washing and drying in a vacuum oven at 80 °C overnight. To formulate MoS_2 macrostructures, samples are typically heated in an inert atmosphere, a procedure not followed in our work. The sample without C_3N_4 was labelled as MS, and the MoS_2/C_3N_4 hybrid sample was labelled as MS/CN.

2.2. Synthesis of C_3N_4 (CN)

C_3N_4 is a carbonaceous material commonly used as a support layer owing to the homogeneous distribution of carbon and heteroatoms in its entirety, a feature that enhances its electrochemical properties (e.g., conductivity). In our work, C_3N_4 was synthesized in a single-step process, by heat treating 10 g of urea (Sigma-Aldrich, 99–100% purity) in a covered alumina crucible at 550 °C for 2 h in an Ar/H_2 atmosphere and at a ramp rate of 5 °C/min. Eventually, we obtained a light, golden-white product, which was marked as C_3N_4. The same product was used in the previously described composite synthesis procedure.

2.3. Synthesis of pine leaf carbon (PLC)

To synthesize highly porous carbon, we followed a previously reported procedure [43]: fresh pine leaves were obtained from a nearby tree (of the *Pinaceae* family), and used as the starting material. The leaves were initially cut into smaller pieces, then washed with water and ethanol, and dried at 80 °C for two days. Subsequently, the leaves were carbonized at 300 °C for 2 h, then ground well and treated with KOH at a 1:5 wt ratio. The mixture was pyrolyzed at 650 °C for 1.5 h under an argon atmosphere. The product was washed with 0.1 M HCl aqueous solution and distilled with water several times to remove the residual K^+ ions. The final product was then vacuum-dried overnight before being used as a component for constructing a hybrid capacitor.

2.4. Material characterization

Crystal structures were characterized by X-ray diffraction (XRD; CuKα radiation, Rint 1000, Rigaku, Japan) in a 2θ range of 5–90°. The particle morphology, elemental composition, and internal structure were evaluated using field emission scanning electron microscopy (FE-SEM, S-4700, Hitachi, Japan) coupled with an energy-dispersive X-ray spectroscopy (EDX) module and high-resolution transmission electron microscopy (HR-TEM; JEM-2000, EX-II, JEOL, Japan). XPS measurements (Multilab 2000, UK) were performed to determine the chemical oxidation sates of Mo, S, C and N on the compound's surface. Raman analysis was conducted (LabRam HR800 UV Raman microscope, Horiba Jobin-Yvon, France) for determining the graphitization of the electrode structure and to confirm the formation of MoS_2. Field emission electron probe micro analysis (FE-EPMA) was performed using JXA-8530F PLUS, with the following testing conditions: beam scan; acc voltage: 15.0 KV; mag: 8000; dwell (ms): 10.00; measured area: 15.00 × 11.25 μm.

2.5. Electrochemical measurements

The electrochemical evaluations of all samples were performed using CR2032 coin cells assembled within a glovebox under a controlled atmosphere of ultrapure argon. The synthesized material and the metallic Na were used as the cathode and anode, respectively, between which a polypropylene separator was employed. Regarding the electrolyte for the sodium ion cell, two aqueous solutions ($NaClO_4$ (1 M) and $LiPF_6$ (1 M)) were mixed in equal volume (1:1) and subsequently added in a mixture of ethylene carbonate (EC) and dimethyl carbonate (DMC) (1 : 1, v/v). The same solvent electrolytes were chosen to ensure optimal mixing. The anode material was coated using the doctor blade method of slurry-coating by maintaining the electrode: carbon: binder ratio at 8:1:1 (Super P® Conductive was used as a conductive carbon and styrene-butadiene rubber/carboxymethylcellulose (SBR/CMC) (1:1 wt%) as a binder). The prepared slurry was coated with copper electrode foil at the required mass loading and dried in an oven at 120 °C overnight prior to cell fabrication. The cathode materials were prepared by mixing 2.5 mg of active materials with 0.5 mg of Ketjenblack EC-300J and 0.5 mg of teflonized acetylene black (TAB-2). The obtained mixtures were pressed on a stainless-steel current collector and dried in an oven at 160 °C for 4 h before cell fabrication. All anode materials were presodiated with sodium metal before constructing the hybrid capacitors. Cyclic voltammetry and electrochemical impedance spectroscopy (EIS) analyses were conducted using an electrochemical analyzer (SP-150, Biologic, France). The scan rate was kept constant at 20 mV s^{-1} unless specified otherwise. Galvanostatic charge-discharge tests were conducted using a battery cycler (WBCS 3000, WonATech) with varying cutoff potentials. The rate performance was evaluated at different current rates (specified in the relevant graph) with 5 cycles per test. EIS was performed on the cells before and after cycling, where the frequency varied from 100 kHz to 10 MHz with an alternating-current amplitude of 10 mV. All measurements were performed at ambient temperature (25 °C).

3. Results and discussions

3.1. Structural and morphological characterizations

X-ray powder diffraction (XRD): The carbon-complex composite, comprising MoS_2 nanocrystals and C_3N_4, was synthesized to achieve larger interlayer distances. Previous researchers have reported the formation of a nanocrystal-derived precipitate [28,44], which was subsequently calcined to form MoS_2 microstructures. Since our objective was synthesizing a compound that would induce a higher interlayer distance, instead of calcinating the nanocrystals (to avoid the microstructure phase), the samples were used without modifications. The resulting structures were analyzed using XRD, according to which the formation of C_3N_4 nanocrystals was confirmed by a broad peak at 27.5° (Fig. 1*a*). For the bare MS sample, the XRD spectra indicated a single low-intensity peak at 10.2°. This was theoretically attributed to the insufficient carbon-complex growth or inadequate MoS_2 crystal development (nucleation seed). Despite the plethora of reported XRD results regarding MoS_2 crystals, almost all of the measured spectra were captured at 2θ ranges of 10° and above, with high-intensity peaks frequently observed near 15°. In our experiment, the C_3N_4-composited sample presented high-intensity peaks at 10.2° (001) and 10.9° (020) (observed with the JCPDS 77–1716) corresponding to the presence of MoS_2, with few other peaks confirming its moiety with ammonia. Müller et al. [45] have extensively investigated this moiety with various spectroscopic techniques. This phenomenon theoretically affirms that the C_3N_4 crystals may have acted as a support pod for MoS_2, which was indicated by additional peaks in the XRD spectra (marked by *). The crystallite size was calculated at 0.87 nm based on the Scherrer equation [46]; this result was in agreement with earlier publications by Gao et al. [47,48], pertaining to MoS_2-induced c-axis expansion.

Electron microscopy (SEM and TEM): The sample morphologies were further analyzed using scanning and transmission electron microscopy (SEM and TEM, respectively; **Figure S-1**). All bare samples appeared as small disks with an average diameter range of 60–90 nm. On the other hand, C_3N_4 crystals appeared as small flakes with a minimum length of 500 nm in at least one direction; their larger surface could have acted as a support pod for Mo and S ions during the hydrothermal process, thus advancing growth. Furthermore, HR-TEM analysis was performed to determine the interlayer distance of the samples, with results confirming the stacking of the layers (Fig. 1e). Regarding the

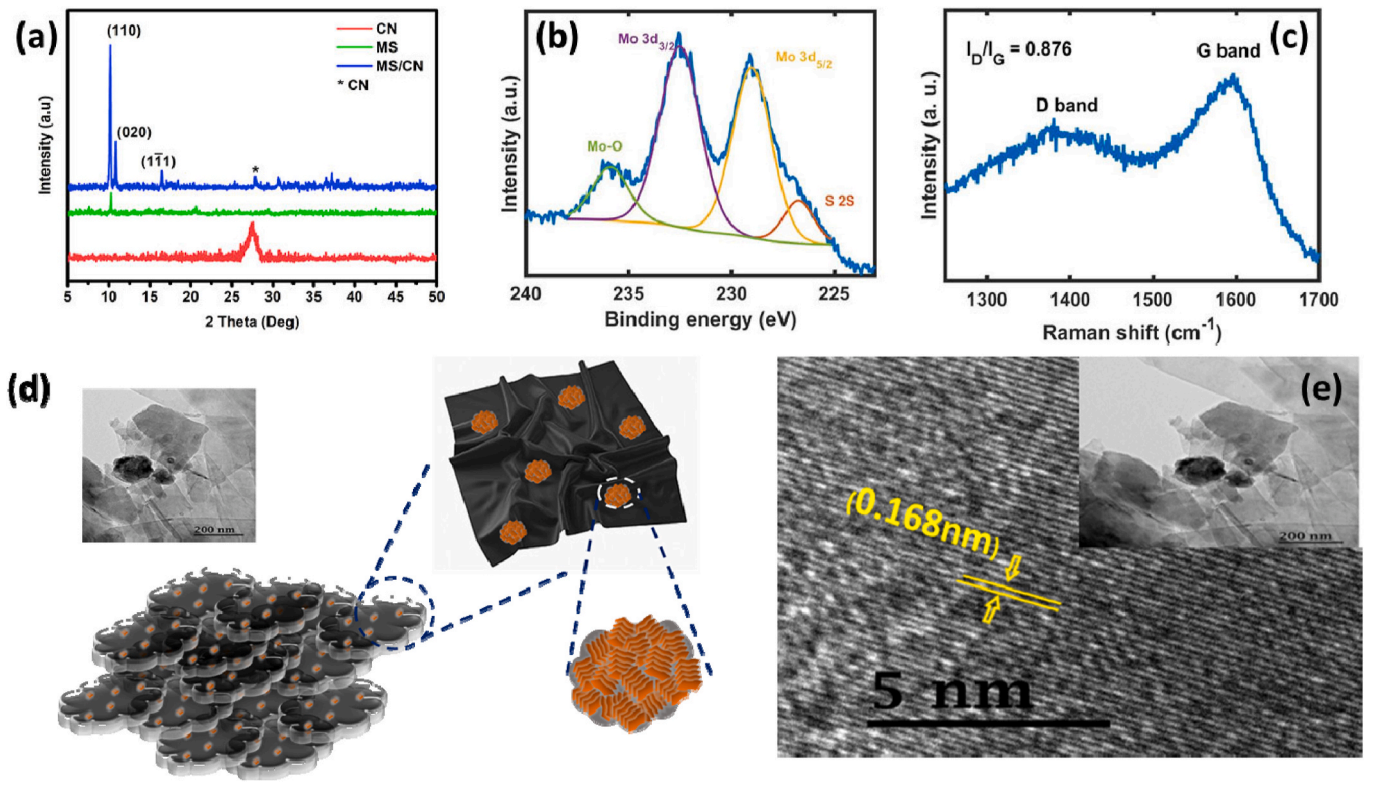

Fig. 1. (a) XRD pattern of anode materials, (b) XPS data of MS/CN, (c) Raman spectrum of MS/CN, (d) Schematic representation of MS/CN with corresponding TEM image on inset, (e) TEM image of MS/CN.

composite samples, due to the coexistence of MoS_2 and C_3N_4, the TEM images could not distinguish the lattice fringes corresponding to MoS_2 and C_3N_4. Hence, based on the measured interlayer distance (0.3 nm), and by comparing it with the corresponding D-spacing value (0.32 nm), the long lattice fringes were identified to belong to C_3N_4. Considering that the bare MoS_2 sample exhibited an interlayer distance comparable with that of the composite sample, the image of the latter was analyzed for reference (**Figure S-2**). Unlike larger particles with lattice fringes, the MS sample presented a sheet-like texture carrying small chunks of nanocrystalline phases with few observed wrinkles. These wrinkles had an interlayer distance of approximately 0.7 nm, which was close to the D-spacing value calculated from the XRD analysis for $2\theta = 10.2^{\circ}$. From the EDX analysis, a homogeneous distribution of all elements was observed (**Figure S-3**); however, traces of carbon and nitrogen in the mapping images suggested that crumbs of carbon sheets with MoS_2 have formed. Based on the microscopic images, a graphical representation of the nanostructure has been recreated (Fig. 1d), with the corresponding TEM image as an inset. To confirm structural integrity, in post mortem analysis TEM images (**Figure S-3**) shows the wrinkles and microcrystalline structures are still intact. But due to presence of binder and electrolyte residues, a clear images could not obtained.

X-ray photoelectron spectrometry (XPS): The XPS analysis results (Fig. 1b) confirmed the presence of Mo, S, C, and N in the surveyed spectra. Further individual peaks were deconvoluted and mapped based on NIST database [49]. The individual peaks show that Mo exhibited two significant peaks at binding energies of 229.1 and 232.3 eV, corresponding to MoS_2; additionally, the sulfur peak at 163.3 eV confirmed the formation of MoS_2. An additional peak at 236.2 eV, corresponding to Mo^{+6} species in MoO_3, suggested that during the nucleation process of MoS_2, small nanocrystals were formed, which were interlinked and induced a graphitic type collapsed structure. The collapsed structure possessed large interlayers, which were reflected in the XRD analysis as well. This feature has multiple advantages that qualify this material as a suitable electrode, such as improved capacity because of the MoS_2 species, and increased conductivity stemming from the carbon crumbles.

Raman spectroscopy: To reaffirm the formation of MoS_2, as well as to better comprehend the layered structures, Raman analysis was performed on the MS/CN sample (Fig. 1c). In accordance with the TEM images, both MS and CN presented a graphitic-type spectrum, with MS/CN having an I_D/I_G ratio of 0.876 (i.e., the system was rendered more graphitic than defective). With regard to obtaining highly conductive C_3N_4 crystals, a high degree of graphitic nature is confirmed to enhance electron transfer; furthermore, the existence of microscopic-scale layers can complement the continuity of the carbon backbone network. As shown in Fig. 1c, other observed bands in phonon mode, such as E^1_{2g} and A_{1g} at 380.5 and 480 cm^{-1}, respectively, reaffirmed the dominant in-plane vibrations of MoS_2 (as opposed to out-of-plane), a typical attribute of few-layered MoS_2 structures. Based on Liang et al.'s report [50], these bands can be interpreted as the unique "fingerprints" of MX_2 (M = Mo, W and X = S), which are also indicative of few-layered MoS_2 structures.

3.2. Half-cell performance

Electrochemical performance of MS/CN anode: The electrode materials were prepared for electrochemical testing using the above-mentioned casting procedure to form a uniformly thick electrode with a Cu current collector an anode and an Al current collector as a cathode.

Upon evaluating different ratios of electrolyte It is observed that, 1:1 (Li:Na) shows the superior conductivity on comparison to 2:1 followed by 1:2 ratios. As stated by Zhang et al. [51] higher conductivity in 1:1 must be attributed to fixed ratio of Li^+/Na^+ which maintains charge neutrality of electrolyte (**Figure S-6**). Hence in this work, 1:1 volumetric ratio was used throughout. To evaluate the performance of the individual electrodes, both electrode materials in the current collectors were coupled with freshly cut Na^+/Na as a counter electrode, with the Na ion and mixed electrolyte undergoing cyclic voltammogram (CV) and galvanostatic charge/discharge cycle (GCD) tests, at a specific current rate,

in a CR2032 cell. Further, the CV curves were drawn in reference to the standard hydrogen electrode (SHE) via manual calculations assuming that the half-cell potentials of Li and Na are −3.04 V and −2.92 V, respectively. Here, the CV potentials (E) were reported vs SHE to avoid confusion with the CV curves taken with different reference metals. The CVs of the anode half cells, i.e. with Li and Na as reference metals (**Figure S-7a**), presented highly comparable characteristics between sodium ions and mixed ions (i.e., in a mixed ion electrolyte) within the potential regime of the Na half-cell, thus implying that Na ions participated more in the intercalation reactions than Lithium ions (which was further affirmed by the less significant peaks of lithium ions in the abovementioned Na half-cell). Furthermore, to determine the impacts of potential lithium deposition regarding the anode in the mixed-ion electrolyte, the anode material was coupled with Li and Na metals and cycled for 5 cycles to allow adequate lithium deposition. An additional reduction peak observed at E exceeding −3.0 V vs SHE (**Figure S-7b**) and the additional oxidation peaks at −0.89 V vs SHE suggested an additional intercalation reaction in the lithium cell configuration.

For the GCD tests, the electrode was swept between 10 and 3000 mV (Fig. 2a). The MoS_2 sample's voltage dropped steadily (resembling a capacitive-type smooth curve), contrary to gradual drops, as commonly observed among battery electrode materials. This smooth GCD curve was in good agreement with earlier reports [35] showing smooth extraction curves below 2.0 V. At a current rate of 0.1 mA g^{-1}, the MS/CN anode exhibited a discharge capacity of 580 mAh g^{-1} in a Na-ion electrolyte. MS/CN anode exhibited a minor hump in the 0.9–0.6 V range with mixed-ion electrolyte because of the delayed ion extraction in the mixed-electrolyte environment, while the MS/CN results delivered a discharge capacity of 572 mAh g^{-1}.

The reaction mechanism when employing a Na^+ electrolyte was as follows:

$$MoS_2 + xNa^+ + xe^- \leftrightarrow Na_xMoS_2 \leftrightarrow \frac{x}{4}Mo + \frac{x}{2}Na_2S + \left(1-\frac{x}{4}\right)MoS_2 \quad (1)$$

The reaction mechanism when employing a mixed-ion (Li^+/Na^+) electrolyte was as follows:

$$MoS_2 + xM^+ + xe^- \leftrightarrow M_xMoS_2 \leftrightarrow \frac{x}{4}Mo + \frac{x}{2}M_2S + \left(1-\frac{x}{4}\right)MoS_2\ (M = Li/Na) \quad (2)$$

To check the capacity retention at higher current rates, the current density was gradually increased until 5 Ag^{-1}. The MS/CN sample was able to retain much of its initial capacity, even after the current increased to 5 Ag^{-1}, with values of 269 mAhhivg^{-1} in a Na-ion electrolyte and 230 mAhg^{-1} in a mixed-ion electrolyte (Fig. 2*b*). This high rate capability was attributed to the faster ion diffusion and wider/smoother pathway for ionic transfer, combined with the increased conductivity induced by the collapsed carbon and highly graphitized

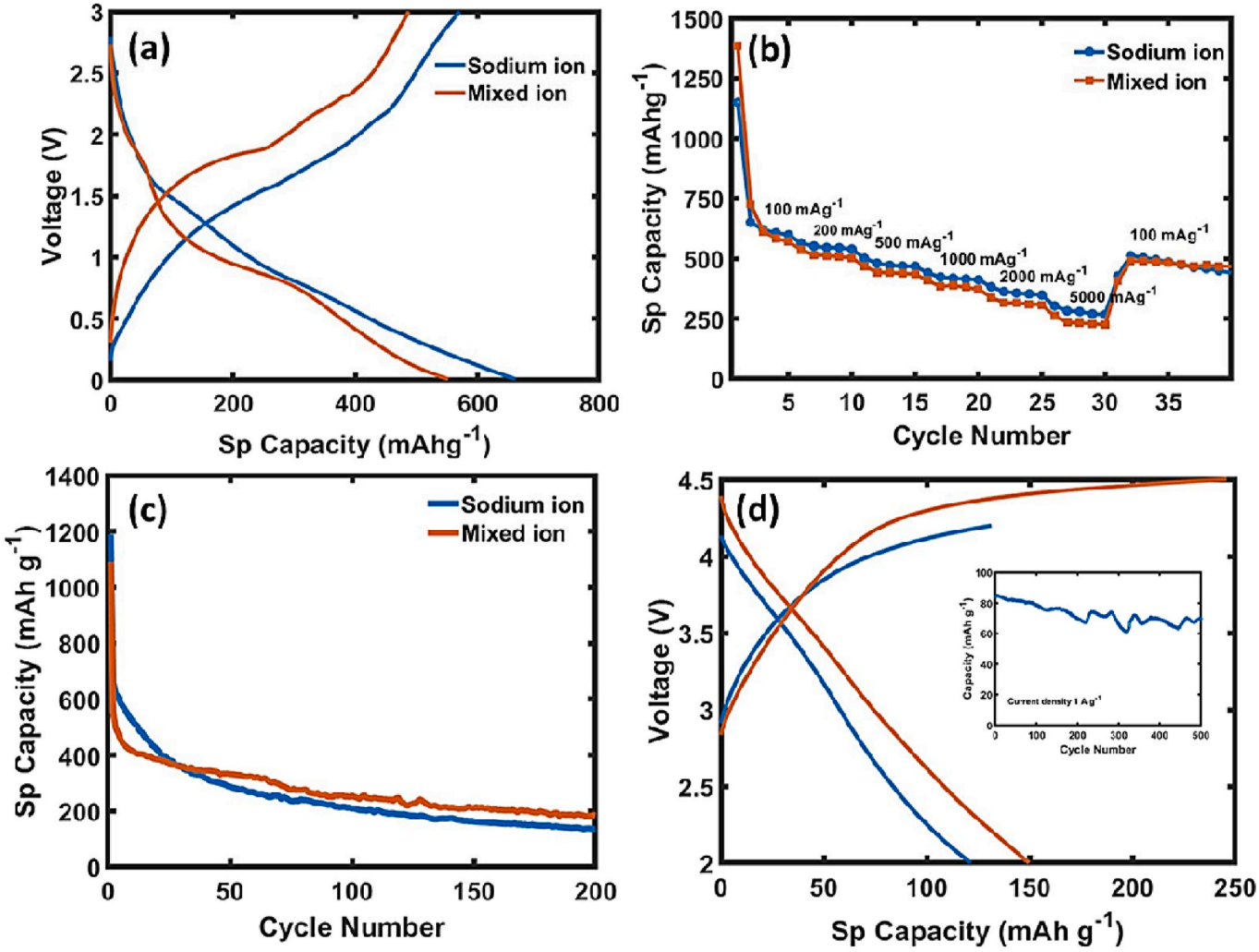

Fig. 2. (a) 2nd cycle charge – discharge performance of MS/CN in different electrolytes at current density of 200 mAg^{-1}, (b) Rate performance of MS/CN in different electrolyte, (c) Cyclic stability of MS/CN at current density of 1Ag^{-1}, (d) 2nd cycle cathodic performance of PLC at different potential window at current density of 200 mAg^{-1} with capacity retention at inset.

nanostructure. When the sodium electrolyte is replaced with the mixed-ion electrolyte, two types of storage mechanisms may arise. In the first type, due to the larger sodium ions occupying additional volume, multiple voids/pores, which could not be accessed by the bulky sodium ions, could be accessed by lithium ions. This can lead to the extraction of additional capacity from the given electrode material. In the second type, the lithium ions that occupied sites accessible to sodium, thus blocking its way, resulted in lesser capacity. The MS/CN sample presented a multistep discharge curve in the sodium-ion electrolyte, as opposed to a smooth discharge pattern (Fig. 2*a*), which was evidently attributed to the severe reduction in capacity caused by the interactions between Li^+ and Na^+ ions. It should be noted that half of the sodium electrolyte volume had been replaced by the lithium electrolyte. Based on the CV curve (**Figure S-7**), a possible explanation could be the second mechanism described above. However, due to the reduced number of larger Na^+ ions, the damage caused to the anode structure was significantly reduced. The same is reflected in Fig. 2c, where the stability curve is smoother and flatter in the mixed-ion electrolyte, in contrast with the gradually decreasing values corresponding to the sodium-ion electrolyte. This kind of capacity loss induced by the presence of MoS_2, especially in a sodium-ion electrolyte, was highly prevalent and had been noticed in previous studies as well [23,24,52]; thus, the improvements reported in this study by replacing the sodium-ion electrolyte with a mixed-ion electrolyte are significant. For comparison Li ion half cells were also tested. From **(Figure S-10)**, though Li ion demonstrated higher initial capacity but stability was poor for Li ion half cell. since our system is modifying an existing Na ion electrolyte system, also aligning ourselves for recent trend of Na replacing Li ion systems we pursued with sodium hybrid capacitor which is the key focus on this work. Additionally, it has been proven that, MoS_2 based hybrid capacitors performs better in sodium electrolyte than Li electrolyte (same has been quoted in introduction) hence studying electrochemical performance in Li ion electrolyte was felt unnecessary.

To better comprehend the mechanism behind the superior performance of a hybrid electrolyte, XPS analysis and field emission electron probe micro analysis (FE-EPMA) were performed on the MS/CN sample at different charge states and varying cycles. MS/CN cycled with sodium metal (sodium-ion and hybrid electrolyte) was analyzed after the 1st discharge (X1D), 1st charge (X1C), 5th Discharge (X5D), and 5th charge (X5C), where the electrolytes used were sodium ion (X = N) and mixed ion (X = M). For comparison purposes, pristine (Pr) MS/CN was also analyzed.

Based on the surveyed spectra (**Figure S-4**), the presence of all elements was confirmed after the 1st discharge, in which, among the spectra of all samples, a prominent Na peak (1071.8 eV) was visible; the peak disappeared during the charge process with the mixed-ion

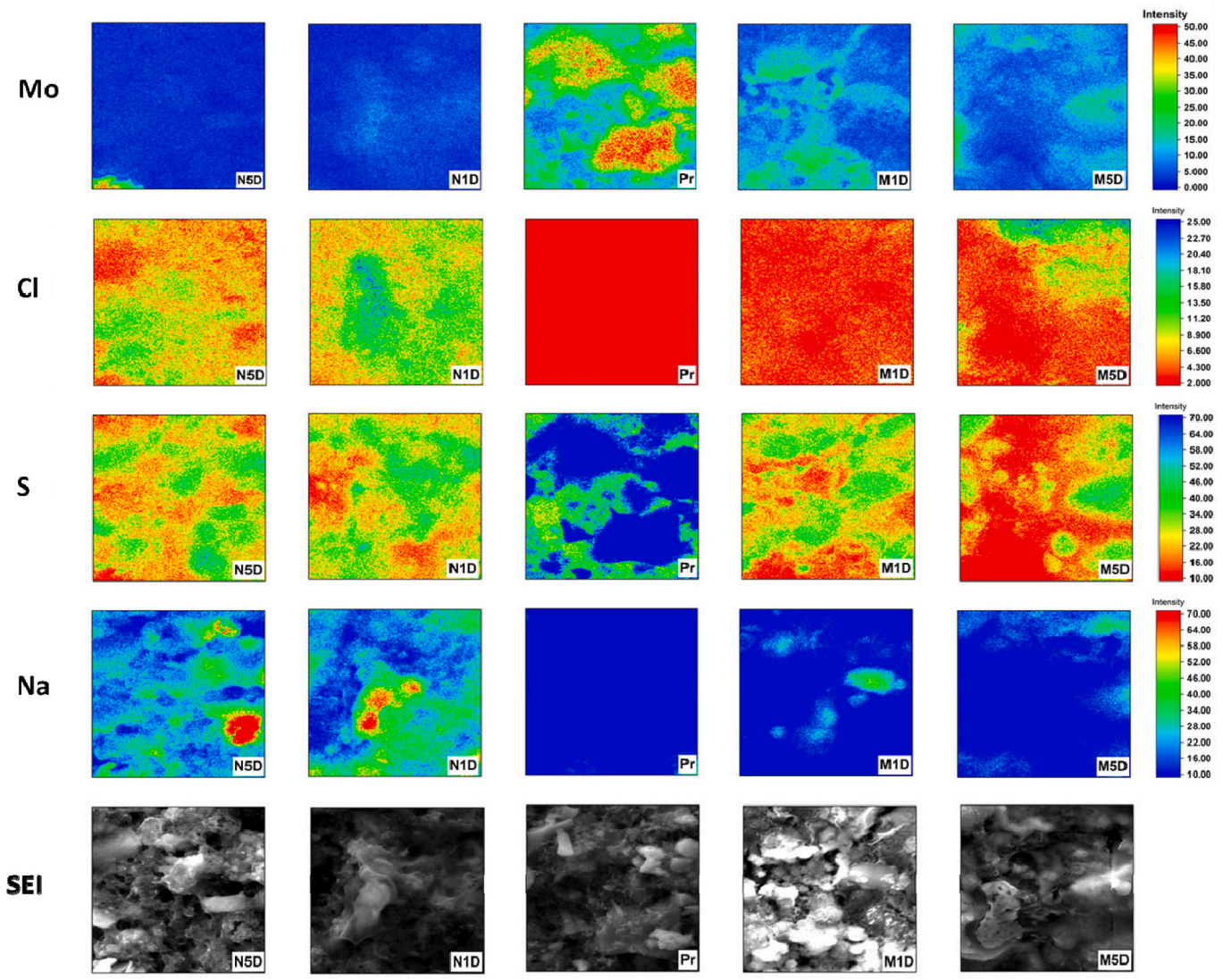

Fig. 3. EPMA mapping of different elements on discharged electrodes analyzed after 1st and 5th cycle; secondary electron image (SEI) of corresponding sample area.

electrolyte (M1C and M5C), but persisted with the sodium-ion electrolyte (N1C and N5C). For maximum coulombic efficiency, the intercalated Na^+ ions should ideally be deintercalated during the charge process. In the case of the Na-ion electrolyte system, a substantial amount of Na^+ has been retained, thus explaining the severe capacity loss between the 1st and 2nd GCD cycles. When normalized, the peak intensity of Na was higher in the sodium-ion electrolyte compared with that in a mixed-ion electrolyte, clearly explaining the reduced storage capacity caused by lithium interactions. This was again clearly evident in EPMA mapping (Fig. 3), in which the presence of sodium in the Na-ion half-cell was apparent even after discharge, whereas only traces were present in the mixed-ion half cells. The average intensity kept increasing from the 1st to the 5th cycle due to repeated addition of sodium in more sites (**Figure S-9**). Though this should yield an increase in capacity, the Na^+ still stuck on the surface during the discharge process resulted in capacity loss. Hence, to further understand the underlying mechanism, the Li/Na ions attached to Mo and S species were analyzed. As stated earlier, two prominent 3d peaks ($3d_{5/2}$ and $3d_{3/2}$) for Mo were observed. Although the peaks appeared at 229.2 and 232.5 eV for the Pr sample corresponding to Mo in the +4 oxidation state, the peak pair shifted to higher binding energies (232.5 and 235.6 eV) via oxidation to the +6-oxidation state. Additionally, the split distance of the peak pair could provide additional information regarding the MoS_2 layer arrangement and its capacity fading mechanism. Based on a computational report by Shu et al. [53], the capacity fading mechanism in MoS_2 was triggered by transitioning from the 2H to the 1T phase, thus slowing down the dissociation of the MoS_2 nanosheets (increasing the binding energy of Mo) and resulting in capacity fading. The aforenoted process was

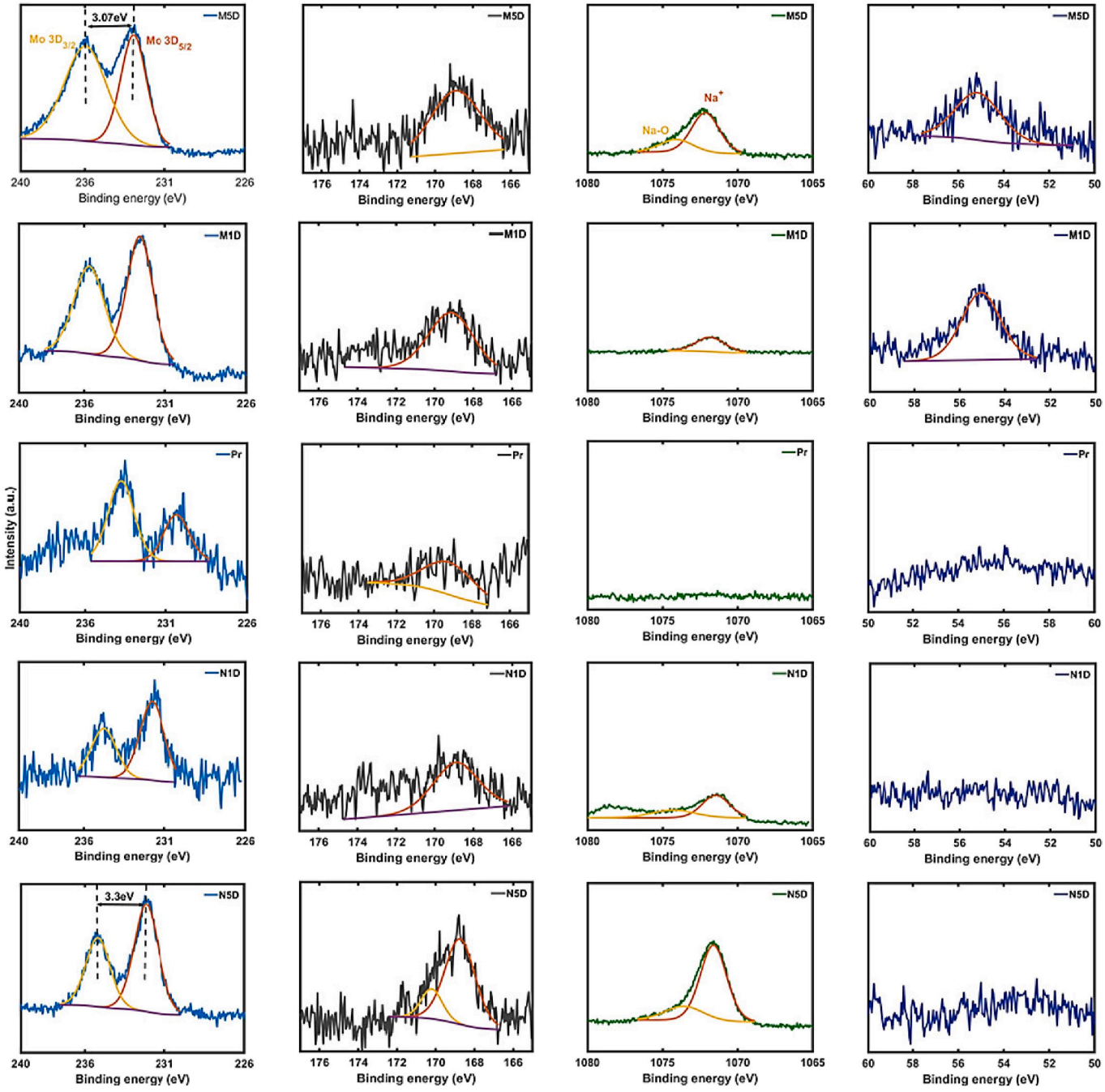

Fig. 4. Elemental XPS spectra of discharged cells at different cycles (Mo-blue; S- grey; Na- Sodium; Li- Violet) with intensities normalized except for Mo spectra. (For interpretation of the references to colour in this figure legend, the reader is referred to the Web version of this article.)

studied with lithium ions; however, the sodium ions used in our work were considerably aggressive. Shu et al. also observed that the top-layer sulfur species were the most affected by this aggressive mechanism and that they were peeled off to the surface. Although it was a computational study, this result was experimentally confirmed in our study by the elemental XPS data and EPMA mapping. The sulfur loss in the Na-ion half-cell may appear marginal (Fig. 4); however, upon close inspection of the Mo mapping, the Mo intensity was observed to fall rapidly in the Na-ion electrolyte, in contrast with that in the mixed-ion electrolyte, implying that an entire layer of Mo and S had been peeled off owing to Na, and an entirely new layer of S had been exposed on the outer surface. In the case of the mixed-ion electrolyte, the Mo and S intensities gradually faded, implying a reduced peeling effect. The slowdown in the dissociation process of MoS_2 could be observed by the increase in the binding energy of the Mo peak pairs, which is in conjunction with the increase in sulfur peak intensity after 5 cycles (which is a better proof for their theory). As a remedy to such degradation, they proposed sandwiching MoS_2 between graphene layers, which was practically impossible. However, since MoS_2 microcrystals are supported on graphitic-type C_3N_4 in the current system, the stability of the anode had been significantly improved. Additionally, based on another computational study by Fan et al. [54], it was computationally confirmed that interlayer coupling lead to the widening of gaps between spin–orbit split states. In our study we observed that the gap between the $3d_{5/2}$ and $3d_{3/2}$ peaks widened to 3.3 eV for the sodium ion case, against 3.07 eV for the mixed ion case. This strongly proves that sulfur layers in MoS_2 nanocrystals are further peeled off. We attempted to reaffirm the changes in the E_{2g} and A_{1g} bands in Raman analysis; however, no strong signals corresponding to these bands could be captured due to interference from other components. Based on the capacity fading results of the computational study by Shu et al. [53] and our experimental findings, a possible degradation mechanism is schematically presented in Fig. 6c. Additionally, in the Li and Na XPS spectra, the intensity of Na kept increasing from the 1st to the 5th cycle in both electrolytes, whereas the Li intensity remained the same during both cycles. This was well in agreement with a computational study by Hao et al. [55], where Li exhibited an adsorption energy of −1.32 eV (lesser than −1.93 eV for Na). Thus, more Na ions are adsorbed and retained in the case of the sodium-ion electrolyte, whereas in the case of the mixed-ion electrolyte, the lithium ion destabilizes the adsorption and desorbs the sodium during the charge process (**Figure S-4**). Although sulfur dissolution is inevitable in MoS_2-based electrodes, it can be reduced in a sodium-ion system by replacing sodium ions with lithium ions and encapsulation inside graphitic structures.

Electrochemical performance of pine leaf carbon cathode: On the other hand, the capacitive-type cathode material (PLC) was tested from 3.0 to 4.2 V vs Na/Na^+ at 100 mAg^{-1}, and the corresponding results are presented in Fig. 2d. The GCD curve was smooth, which was typical for a

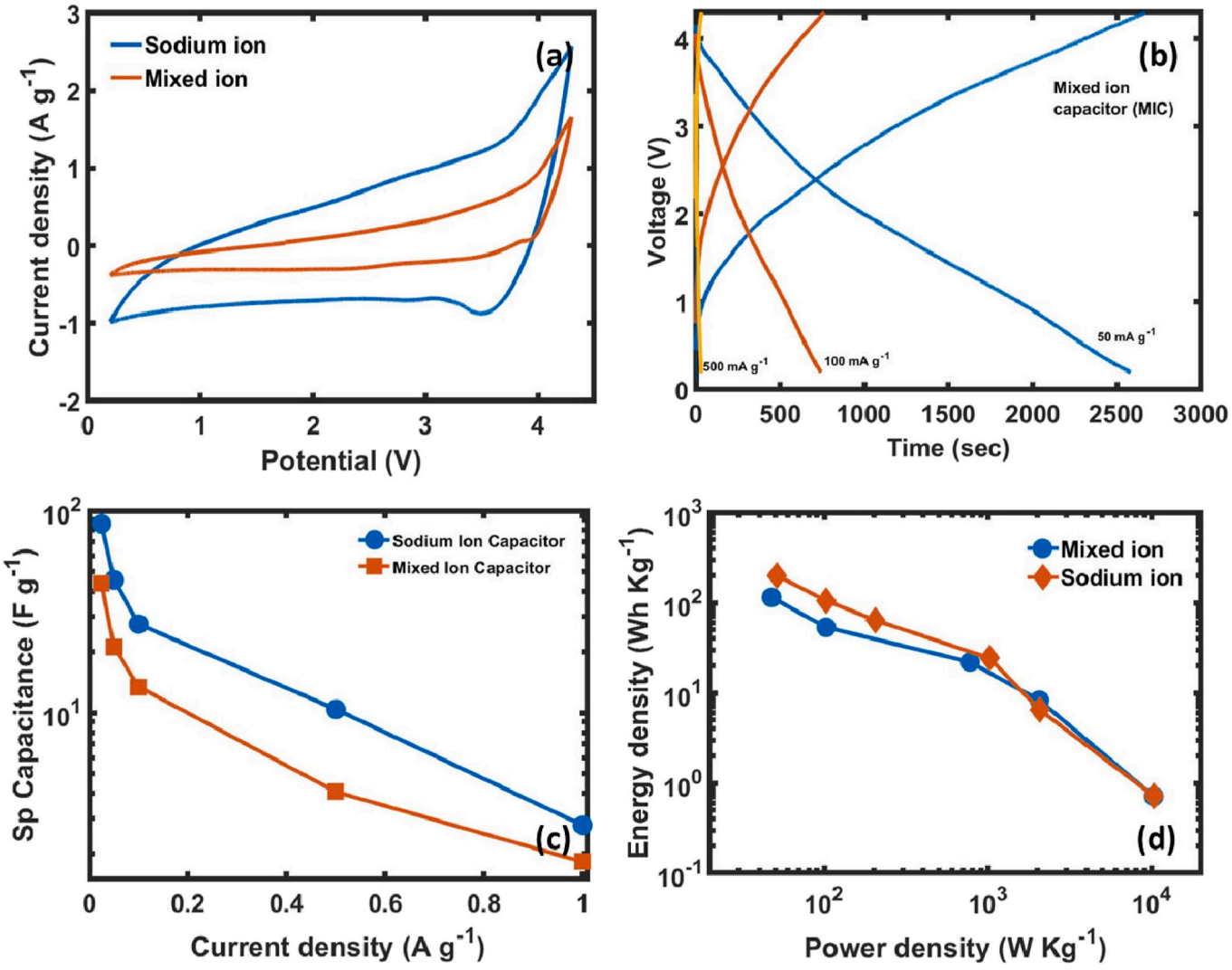

Fig. 5. (a) CV comparison for hybrid capacitors with different electrolytes, (b) GCD of mixed-ion hybrid capacitor, (c) Capacitance of hybrid capacitor in different electrolytes, (d) Ragone plot for hybrid capacitor (similar loading indicated by line and markers).

capacitive-type material exhibiting a surface-dominant charge/discharge process. Similar, surface dominant characteristics was observed in few other earlier reports too [56,57]. Though in earlier reports capacity faded with higher current density, here it could deliver a capacity of 120 $mAhg^{-1}$ and did not fade significantly with higher current densities, suggesting a highly reversible physisorption process. This improved performance can be attributed to optimized synthesized procedure which made it highly porous and carbon material's high compatibility in current system. Though the cathode endured higher potentials until 4.5 V (Fig. 2d), the polarization of GCD began after 4.3 V, and hence, the upper cutoff was set as 4.2 V. PLC was chosen against conventional activated carbon due to its specific capacity, which was at least 20% higher. Its advantages as a hybrid capacitor were that it was lighter and thinner, because a lesser mass loading is required. Many studies have emphasized on the electrode material for the anode; however, the cathode should also be given equal importance for improving hybrid capacitors. Upon increasing the current rate, the capacitance further dropped (Fig. 5c) in full cell hybrid capacitor. The poor anode architecture led to poor specific capacitance at higher current density. Since various previous reports mainly focused on architectures such as ultrathin, nanoflower and interlayer expanded etc. and these architectures improved both capacity and diffusivity of ions. But for practical application such strategies are difficult to be followed since these architectures are very much sensitive to such temperatures and other parameters during synthesis. Hence, we took a MoS_2 with simplest synthesis method and architecture which is susceptible for poor performance and least resistance to structural damage. we mainly focused on improving stability in a vulnerable architecture and hence the electrochemical performance at higher current density is not on par.

Sodium ion vs mixed ion/hybrid capacitor: In extending this phenomenon to construct highly efficient hybrid capacitors, a proper mass balance must be achieved between the cathode and the anode. Li hybrid capacitors perform better than their Na equivalents in most cases, mainly because of their smaller ionic size (among other properties). Hence, many groups have worked on mixed-ion electrolytes (i.e. Li and Na ions mixed in equal ratio) to increase energy densities in battery systems [58] [–] [61]. To the best of our knowledge, this idea has been never been extended to a hybrid capacitor system. It was assumed that the addition of Li ions to the electrolyte would enable the extraction of additional energy and capacity from the electrode materials, as well as yield wider potential ranges. Although the aforementioned properties were expected, the actual underlying mechanism was unexplored. Hence, a mixed-ion electrolyte was formulated as described earlier. Hybrid capacitors using sodium ions and mixed ions were constructed and tested simultaneously. The fabricated sodium hybrid capacitor (NHC) was tested between 0.2 and 4.2 V to evaluate its electrochemical performance. Similarly, a mixed-ion capacitor (MIC) was constructed and tested between 0.2 and 4.2 V to evaluate its electrochemical performance. Based on the capacity at a given current rate, the mass balance between the anode and cathode was achieved, with a factor of 3.8. The voltage window was decided according to the cyclic voltammetry (CV) curve and GCD. The cell window was cut off at potentials well below the voltage at which dv/dt increased exponentially. The CV curve (Fig. 5a) featured a hysteresis-type smooth curve with a reduction peak

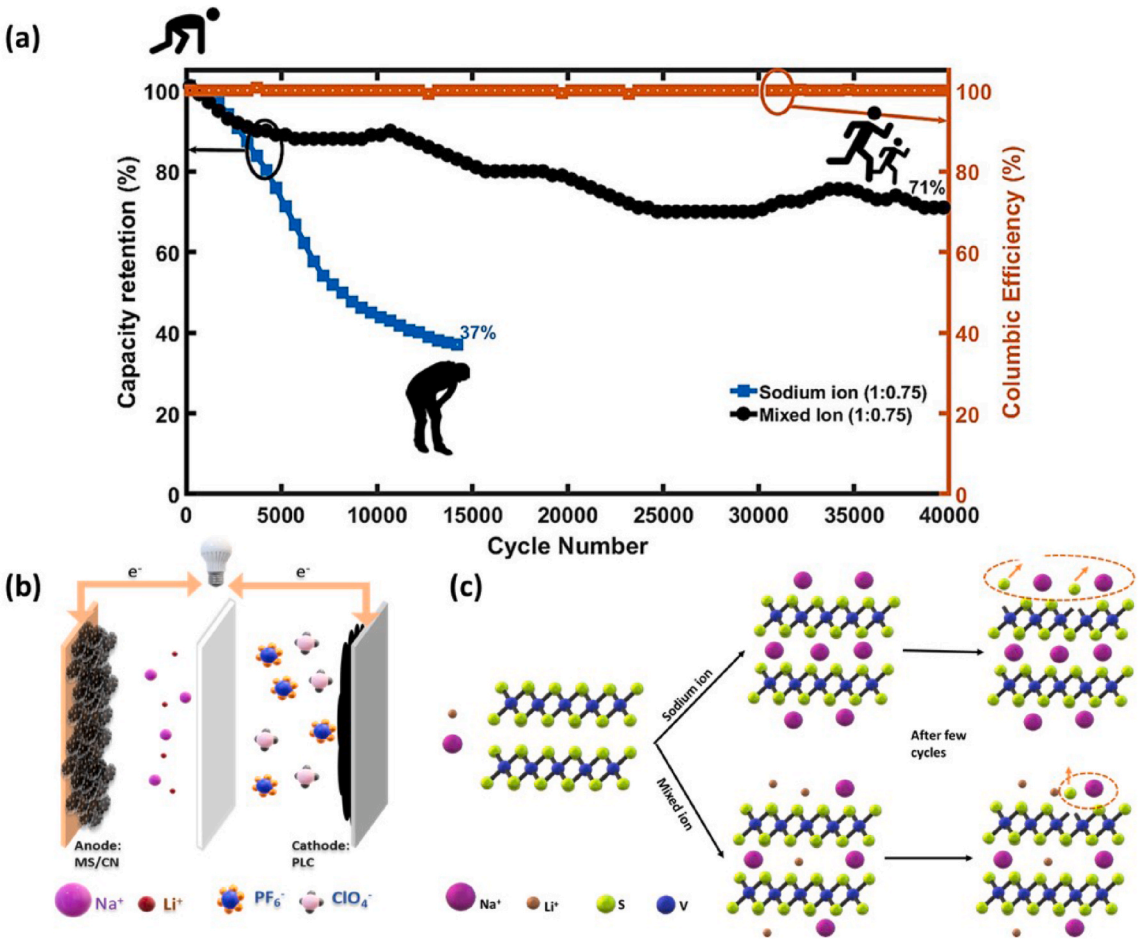

Fig. 6. (a) Cyclic stability of hybrid capacitor with same mass balance in sodium ion electrolyte and mixed ion electrolyte (Current density: 1 Ag^{-1}), (b) Schematic of hybrid capacitor, (c) Schematic representation of sulfur (green balls) dissolution effect in anode. (For interpretation of the references to colour in this figure legend, the reader is referred to the Web version of this article.)

at 3.49 V arising from intercalation reactions. Negligible bumps or peaks are observed in both the cathodic and anodic sweeps, with merely gradual increases in current density clearly indicating the smooth charge–discharge process. The same is reflected in the smooth GCD curve. At a given scan rate, the normalized CV curve presented higher current densities for the sodium-ion electrolyte than those for the mixed-ion electrolyte, indicating the reduced capacitance in the MIC. Although no reduction peaks were observed in the CV for HC, the exact mechanism occurring at the anode and cathode halves in the HC configuration is unknown. The high-intensity reduction peak corresponding to the mixed-ion Li half-cell at lower potentials could explain the polarization observed at higher potentials (exceeding 4 V) in GCD, as well as generate additional capacity.

The mechanism discussed above was also reflected in the smooth triangular GCD curves. Fig. 5b shows the GCD at different current densities. The obtained curve was smooth for both the sodium ion and mixed ion configurations, unlike the stepped curve obtained for the half-cell with the mixed ion electrolyte. Based on the GCD curve, the charge storage appeared to be a smooth process owing to the smaller MS nanocrystals. The calculated energy and power density values for a given hybrid capacitor were comparable with those of an equivalent battery or a supercapacitor in the corresponding regimes. In Fig. 5b, it can be noted that polarization occurred at higher voltages and the curve tended to flatten. In the same regime, no significant polarization was observed in the sodium-ion capacitor. This could be because of slight deposition of the lithium ions present in the mixed-ion electrolyte, which could have significantly shifted the corresponding half-cell potentials. When NHC was charged initially, Na^+ ions intercalated into the anode, and the anions were simultaneously adsorbed into the carbon cathode, forming an electric double layer capacitor (EDLC). During discharge, desorption and deintercalation of ions to the electrolyte occurred, thus confirming that the entire process was highly reversible. This combination of processes occurring in a battery-type anode and capacitive-type cathode contributed to the high energy and power densities of NHC. A schematic diagram of the aforementioned processes has been presented in Fig. 6b.

The results showed that the fabricated NHC and MIC delivered high discharge capacities, as well as extraordinary stability, as shown in Fig. 6b. To best of our knowledge, this was the first HC with a mixed ion electrolyte, i.e. two anions and two cations. Our approach was different from the multi-ion strategy followed by Liu et al.'s group [62], which utilized only one cation and in which the second anions were not alkali ions. Although NHC outperformed several MoS_2-based sodium hybrid capacitors [27,33,63,64], MICs have also outperformed some sodium hybrid capacitors (see Table 1). The suitability of the proposed HC for practical application is shown by a Ragone plot. A high energy density of 172 Wh Kg^{-1} was achieved at a specific power of 51.07 W kg^{-1} along with a maximum power density of up to 10287 W kg^{-1}. Similarly, our MIC also achieved a high energy density of 124 Wh Kg^{-1} at the specific power of 47 W kg^{-1}. Although NHC exhibited substantially high energy and power densities, it was adversely affected by poor cycle stability; further, it severely lost its capacity after 10000 cycles. Hence, this system can be considered ideal for our study. NHC lost 50% of its initial capacity by 10000 cycles and broke down after 17000 cycles owing to the larger Na ions and tiny microcrystals of MoS_2. In contrast, when similarly, mass balanced MIC was checked for cycle stability, it could retain 71% of its initial capacity even after 40000 cycles. It can be understood from the Ragone plot (Fig. 5d) that at this ratio (1:0.75), the MIC was not properly balanced. When balanced adequately, owing to the change in anode capacity arising from the mixed electrolyte, it could achieve greater capacity retention after 40000 cycles. This superior performance was attributed to the combination of MS/CN, PLC, and the MIC electrolyte. This clearly demonstrates that NHC outperformed several sodium hybrid capacitors, and that the novel MIC exhibited exceptional stability. If the Na:Li ion ratio is further optimized, the capacity could be improved, such that it is similar to that of NHC, with superior stability. To understand the superior performance, the cell that operated for 40000 cycles was analyzed via EIS and the corresponding Nyquist plot has been shown in **Figure S-8**. The initially high resistance of the MIC explained the capacity loss, but after the last cycle, the increase in resistance was less compared with that in the sodium ion case, thus yielding the superior cycle stability of the MIC. Additionally, in **(Figure S-2c and d)** the structural integrity was verified. Even after 40000 cycles, the wrinkles and microcrystalline domains were retained owing to smooth charge storage process by mixed ion electrolyte.

Based on the results of the comparison between NHC and the MIC, the following observations are made: (i) Equal performance at higher current density: Although the capacity and energy density were low at lower current rates, the MIC exhibited better energy and power performance at higher current rates, as shown in the Ragone plot (Fig. 5d). (ii) Cycle stability can be drastically improved: Since the bulky Na + ions can wear the microstructures, they can be replaced with Li ions. (iii) Highly efficient nanocrystal architecture: As observed in the half cell and full cell studies, capacity is largely associated with the anode material, and the nanocrystal architecture greatly facilitated faster ion and electron transfer via the graphitic CN backbone. (iv) Advantages of MIC over NHC: The advantages of Li and Na hybrid capacitors are well known; nonetheless, for better performance, hybrid capacitors require prelithiation or Sodiation, which entails solid metals. Presodiation is safer and cheaper than prelithiation. However, the advantages of lithium ions over sodium ions with regard to higher capacity and stability are highly beneficial. Notably, the proposed MIC can achieve optimal results by using a presodiation process in addition to extracting additional energy using lithium ions. As mentioned earlier, even sites that are no longer accessible by sodium can be reused by lithium, and eventually, the capacity is not compromised. More simply, lithium acts as a "little brother" to sodium rather than as its rival.

Table 1
Comparison with few earlier reports on MoS_2 based anode.

Anode	Electrolyte	Maximum Energy density [Wh Kg^{-1}]	Maximum Cycle number reported	References
MoS_2/C_3N_4	$NaClO_4$	172	15000	Our work
MoS_2/C_3N_4	Mixed ion	124	40000	Our work
MoS_2-Carbon Monolayer	$NaClO_4$	111	10000	[65]
Interlayer - expanded MoS_2/rGO composite	$NaClO_4$	140	10000	[66]
Ultrathin MoS_2 nanosheet	$NaClO_4$	112	5000	[33]
PCNF@MoS_2@PEDOT double core/shell nanofiber electrode	Gel electrolyte	130	5000	[67]
MoS_2/CoS_2-RGO	$NaClO_4$	152	100	[68]

4. Conclusion

To replace sodium with a mixed-ion electrolyte in SICs, a novel capacitor with an MoS_2-based nanocrystal architecture was successfully constructed using a CN graphitic backbone as an anode and a PLC porous material as a capacitive cathode. This novel system delivered a significant energy value of 172.38 Wh kg^{-1} in a sodium electrolyte configuration and 124.5 Wh kg^{-1} in a mixed-ion electrolyte configuration. Furthermore, when a mixed-ion electrolyte was employed, a notably superior (compared with sodium electrolyte) cycle performance was achieved (up to 40000 cycles). To the best of our knowledge, this is the first research to provide successful test results for such a MIC. This innovative hybrid system exhibits substantial potential for application in high-energy and high-power energy storage systems. The degradation mechanism of the anode material was well comprehended via thorough and systematic studies using XPS, as well as based on the agreement of

our experimental results with those of various computational studies; however, further studies with other electrode materials and electrolyte ratios are required, since several variables remain unexplored. The authors welcome any suggestions and insights for improving our collective understanding in this regard.

Author contributions

The manuscript was written through contributions of all authors. All authors have given approval to the final version of the manuscript.

CRediT authorship contribution statement

Bala Krishnan Ganesan: Conceptualization, Methodology, Formal analysis, Investigation, Software, Visualization, Writing – original draft. **Ranjith Thangavel:** Methodology, Formal analysis, Investigation, Visualization, Writing – review & editing. **Megala Moorthy:** Methodology, Formal analysis, Investigation. **Seo - Jun Lee:** Methodology, Formal analysis, Investigation. **Won-Sub Yoon:** Resources, Supervision, Validation. **Yun-Sung Lee:** Funding acquisition, Resources, Supervision, Visualization, Validation, Writing – review & editing.

Declaration of competing interest

The authors declare that they have no known competing financial interests or personal relationships that could have appeared to influence the work reported in this paper.

Acknowledgment

This work was supported by the National Research Foundation of Korea (NRF) grant funded by the Korean government (Ministry of Science, ICT & Future Planning) (No. 2019R1A4A2001527). Dr. Ranjith Thangavel acknowledges the support from the National Research Foundation of Korea (NRF) grant funded by the Korea government (MSIT) (No. 2020R1C1C1014961). The authors would like to thank Dr Kalpana Dharmalingam, CECRI, Chennai Unit for her valuable discussions.

Appendix A. Supplementary data

Supplementary data to this article can be found online at https://doi.org/10.1016/j.jpowsour.2021.229918.

References

[1] J. Kim, A. Manthiram, A manganese oxylodide cathode for rechargeable lithium batteries, Nature 390 (1997) 265–267, https://doi.org/10.1038/36812.
[2] R. Thangavel, A.G. Kannan, R. Ponraj, X. Sun, D.W. Kim, Y.S. Lee, Highly interconnected hollow graphene nanospheres as an advanced high energy and high power cathode for sodium metal batteries, J. Mater. Chem. A. 6 (2018) 9846–9853, https://doi.org/10.1039/c8ta00153g.
[3] S. Wang, J. Zhao, L. Wang, X. Liu, Y. Wu, J. Xu, High performance $Na_3V_2(PO_4)_3$/C composite electrode for sodium-ion capacitors, Ionics 21 (2015) 2633–2638, https://doi.org/10.1007/s11581-015-1428-9.
[4] R. Thangavel, K. Kaliyappan, K. Kang, X. Sun, Y.S. Lee, Going beyond lithium hybrid capacitors: proposing a new high-performing sodium hybrid capacitor system for next-generation hybrid vehicles made with bio-inspired activated carbon, Adv. Energy Mater. 6 (2016) 1–9, https://doi.org/10.1002/aenm.201502199.
[5] D. Guo, J. Qin, Z. Yin, J. Bai, Y.K. Sun, M. Cao, Achieving high mass loading of $Na_3V_2(PO_4)_3$@carbon on carbon cloth by constructing three-dimensional network between carbon fibers for ultralong cycle-life and ultrahigh rate sodium-ion batteries, Nano Energy 45 (2018) 136–147, https://doi.org/10.1016/j.nanoen.2017.12.038.
[6] R. Thangavel, B. Moorthy, D.K. Kim, Y.S. Lee, Pushing the energy output and cyclability of sodium hybrid capacitors at high power to new limits, Adv. Energy Mater. 7 (2017), https://doi.org/10.1002/aenm.201602654.
[7] H.K. Roh, M.S. Kim, K.Y. Chung, M. Ulaganathan, V. Aravindan, S. Madhavi, K. C. Roh, K.B. Kim, A chemically bonded $NaTi_2(PO_4)_3$/rGO microsphere composite as a high-rate insertion anode for sodium-ion capacitors, J. Mater. Chem. A. 5 (2017), https://doi.org/10.1039/c7ta05252a.
[8] T. Wei, G. Yang, C. Wang, Iso-Oriented $NaTi_2(PO_4)_3$ mesocrystals as anode material for high-energy and long-durability sodium-ion capacitor, ACS Appl. Mater. Interfaces 9 (2017), https://doi.org/10.1021/acsami.7b08778.
[9] Z. Zhou, N. Li, C. Zhang, X. Chen, F. Xu, C. Peng, Preparation of carbon layer and carbon nanotube co-decorated $NaTi_2(PO_4)_3$ anode and its application in sodium-ion batteries, Solid State Ionics 324 (2018), https://doi.org/10.1016/j.ssi.2018.06.011.
[10] Q. Yang, S. Cui, Y. Ge, Z. Tang, Z. Liu, H. Li, N. Li, H. Zhang, J. Liang, C. Zhi, Porous single-crystal $NaTi_2(PO_4)_3$ via liquid transformation of TiO_2 nanosheets for flexible aqueous Na-ion capacitor, Nano Energy 50 (2018), https://doi.org/10.1016/j.nanoen.2018.06.017.
[11] D. Guo, J. Qin, C. Zhang, M. Cao, Constructing flexible and binder-free $NaTi_2(PO_4)_3$ film electrode with a sandwich structure by a two-step graphene hybridizing strategy as an ultrastable Anode for long-life sodium-ion batteries, Cryst. Growth Des. 18 (2018), https://doi.org/10.1021/acs.cgd.7b01549.
[12] D. Chao, C.H.M. Lai, P. Liang, Q. Wei, Y.S. Wang, C.R. Zhu, G. Deng, V.V.T. Doan-Nguyen, J. Lin, L. Mai, H.J. Fan, B. Dunn, Z.X. Shen, Sodium vanadium fluorophosphates (NVOPF) array cathode designed for high-rate full sodium ion storage device, Adv. Energy Mater. 8 (2018), https://doi.org/10.1002/aenm.201800058.
[13] M. Arnaiz, J.L. Gómez-Cámer, J. Ajuria, F. Bonilla, B. Acebedo, M. Jáuregui, E. Goikolea, M. Galceran, T. Rojo, High performance titanium antimonide $TiSb_2$ alloy for Na-ion batteries and capacitors, Chem. Mater. 30 (2018), https://doi.org/10.1021/acs.chemmater.8b02639.
[14] M.C. Liu, H. Zhang, Y.X. Hu, C. Lu, J. Li, Y.G. Xu, L. Bin Kong, Special layer-structured WS_2 nanoflakes as high performance sodium ion storage materials, Sustain. Energy Fuels (2019), https://doi.org/10.1039/c9se00047j.
[15] X. Zeng, Z. Ding, C. Ma, L. Wu, J. Liu, L. Chen, D.G. Ivey, W. Wei, Hierarchical nanocomposite of hollow N-doped carbon spheres decorated with ultrathin WS_2 nanosheets for high-performance lithium-ion battery anode, ACS Appl. Mater. Interfaces 8 (2016) 18841–18848, https://doi.org/10.1021/acsami.6b04770.
[16] M.C. Liu, H. Zhang, Y.X. Hu, C. Lu, J. Li, Y.G. Xu, L. Bin Kong, Special layer-structured WS_2 nanoflakes as high performance sodium ion storage materials, Sustain. Energy Fuels. 3 (2019), https://doi.org/10.1039/c9se00047j.
[17] Y. Wang, X. Zhang, P. Xiong, F. Yin, Y. Xu, B. Wan, Q. Wang, G. Wang, P. Ji, H. Gou, Insight into the intercalation mechanism of WSe_2 onions toward metal ion capacitors: sodium rivals lithium, J. Mater. Chem. A. 6 (2018), https://doi.org/10.1039/c8ta09286a.
[18] S. Ito, S. Tanaka, K. Manabe, H. Nishino, Effects of surface blocking layer of Sb_2S_3 on nanocrystalline TiO_2 for $CH_3NH_3PbI_3$ perovskite solar cells, J. Phys. Chem. C (2014), https://doi.org/10.1021/jp500449z.
[19] S. Liu, Z. Cai, J. Zhou, M. Zhu, A. Pan, S. Liang, High-performance sodium-ion batteries and flexible sodium-ion capacitors based on Sb_2X_3 (X = O, S)/carbon fiber cloth, J. Mater. Chem. A. 5 (2017), https://doi.org/10.1039/c7ta01895a.
[20] Z. Xia, H. Sun, X. He, Z. Sun, C. Lu, J. Li, Y. Peng, S. Dou, J. Sun, Z. Liu, In situ construction of $CoSe_2$ @vertical-oriented graphene arrays as self-supporting electrodes for sodium-ion capacitors and electrocatalytic oxygen evolution, Nano Energy (2019), https://doi.org/10.1016/j.nanoen.2019.03.052.
[21] V.V.T. Doan-Nguyen, S. Zhang, E.B. Trigg, R. Agarwal, J. Li, D. Su, K.I. Winey, C. B. Murray, Synthesis and X-ray characterization of cobalt phosphide (Co_2P) nanorods for the oxygen reduction reaction, ACS Nano 9 (2015) 8108–8115, https://doi.org/10.1021/acsnano.5b02191.
[22] R. Thangavel, A. Samuthira Pandian, H.V. Ramasamy, Y.S. Lee, Rapidly synthesized, few-layered pseudocapacitive SnS_2 anode for high-power sodium ion batteries, ACS Appl. Mater. Interfaces 9 (2017) 40187–40196, https://doi.org/10.1021/acsami.7b11040.
[23] X. Zhang, J. Xiang, C. Mu, F. Wen, S. Yuan, J. Zhao, D. Xu, C. Su, Z. Liu, SnS_2 nanoflakes anchored graphene obtained by liquid phase exfoliation and MoS_2 nanosheet composites as lithium and sodium battery anodes, Electrochim. Acta 227 (2017) 203–209, https://doi.org/10.1016/j.electacta.2017.01.036.
[24] T. Stephenson, Z. Li, B. Olsen, D. Mitlin, Lithium ion battery applications of molybdenum disulfide (MoS_2) nanocomposites, Energy Environ. Sci. 7 (2014) 209–231, https://doi.org/10.1039/c3ee42591f.
[25] J. Ding, W. Hu, E. Paek, D. Mitlin, Review of hybrid ion capacitors: from aqueous to lithium to sodium, Chem. Rev. (2018), https://doi.org/10.1021/acs.chemrev.8b00116.
[26] J. Kibsgaard, J.V. Lauritsen, E. Lægsgaard, B.S. Clausen, H. Topsøe, F. Besenbacher, Cluster-support interactions and morphology of MoS_2 nanoclusters in a graphite-supported hydrotreating model catalyst, J. Am. Chem. Soc. 128 (2006) 13950–13958, https://doi.org/10.1021/ja0651106.
[27] C. Zhan, W. Liu, M. Hu, Q. Liang, X. Yu, Y. Shen, R. Lv, F. Kang, Z.H. Huang, High-performance sodium-ion hybrid capacitors based on an interlayer-expanded MoS_2/rGO composite: surpassing the performance of lithium-ion capacitors in a uniform system, NPG Asia Mater. (2018) 775–787, https://doi.org/10.1038/s41427-018-0073-y.
[28] J. Tian, H. Zhang, Z. Li, Synthesis of double-layer nitrogen-doped microporous hollow carbon@MoS_2/MoO_2 nanospheres for supercapacitors, ACS Appl. Mater. Interfaces 10 (2018) 29511–29520, https://doi.org/10.1021/acsami.8b08534.
[29] Z. Hu, L. Wang, K. Zhang, J. Wang, F. Cheng, Z. Tao, J. Chen, MoS_2 nanoflowers with expanded interlayers as high-performance anodes for sodium-ion batteries, Angew. Chem. 126 (2014) 13008–13012, https://doi.org/10.1002/ange.201407898.
[30] D. Su, S. Dou, G. Wang, Ultrathin MoS_2 nanosheets as anode materials for sodium-ion batteries with superior performance, Adv. Energy Mater. 5 (2015), https://doi.org/10.1002/aenm.201401205.

[31] Y. Tang, Z. Zhao, Y. Wang, Y. Dong, Y. Liu, X. Wang, J. Qiu, Ultrasmall MoS_2 nanosheets mosaiced into nitrogen-doped hierarchical porous carbon matrix for enhanced sodium storage performance, Electrochim. Acta 225 (2017) 369–377, https://doi.org/10.1016/j.electacta.2016.12.176.

[32] M. Xu, F.L. Yi, Y. Niu, J. Xie, J. Hou, S. Liu, W.H. Hu, Y. Li, C.M. Li, Solvent-mediated directionally self-assembling MoS_2 nanosheets into a novel worm-like structure and its application in sodium batteries, J. Mater. Chem. A. 3 (2015) 9932–9937, https://doi.org/10.1039/c5ta00315f.

[33] Y. Li, H. Wang, B. Huang, L. Wang, R. Wang, B. He, Y. Gong, X. Hu, Mo_2C-induced solid-phase synthesis of ultrathin MoS_2 nanosheet arrays on bagasse-derived porous carbon frameworks for high-energy hybrid sodium-ion capacitors, J. Mater. Chem. A. 6 (2018) 14742–14751, https://doi.org/10.1039/c8ta04597f.

[34] M. Tahir, C. Cao, N. Mahmood, F.K. Butt, A. Mahmood, F. Idrees, S. Hussain, M. Tanveer, Z. Ali, I. Aslam, Multifunctional g-C_3N_4 nanofibers: a template-free fabrication and enhanced optical, electrochemical, and photocatalyst properties, ACS Appl. Mater. Interfaces 6 (2014) 1258–1265, https://doi.org/10.1021/am405076b.

[35] H. Zhu, F. Zhang, J. Li, Y. Tang, Penne-like MoS_2/carbon nanocomposite as anode for sodium-ion-based dual-ion battery, Small 14 (2018) 1703951, https://doi.org/10.1002/smll.201703951.

[36] J. Barker, R.K.B. Gover, P. Burns, A.J. Bryan, Hybrid-ion: a lithium-ion cell based on a sodium insertion material, Electrochem. Solid State Lett. 9 (2006) A190, https://doi.org/10.1149/1.2168288.

[37] N.V. Kosova, D.O. Rezepova, S.A. Petrov, A.B. Slobodyuk, Electrochemical and chemical Na^+/Li^+ ion exchange in Na-based cathode materials: $Na_{1.56}Fe_{1.22}P_2O_7$ and $Na_3V_2(PO_4)_2F_3$, J. Electrochem. Soc. 164 (2017) A6192–A6200, https://doi.org/10.1149/2.0301701jes.

[38] W. Song, X. Ji, C. Pan, Y. Zhu, Q. Chen, C.E. Banks, A $Na_3V_2(PO_4)_3$ cathode material for use in hybrid lithium ion batteries, Phys. Chem. Chem. Phys. 15 (2013) 14357–14363, https://doi.org/10.1039/c3cp52308j.

[39] J.P. Baboo, J. Song, S. Kim, J. Jo, S. Baek, V. Mathew, D.T. Pham, M.H. Alfaruqi, Z. Xiu, Y.K. Sun, J. Kim, Monoclinic-orthorhombic $Na_{1.1}Li_{2.0}V_2(PO_4)_3$/C composite cathode for Na^+/Li^+ hybrid-ion batteries, Chem. Mater. 29 (2017) 6642–6652, https://doi.org/10.1021/acs.chemmater.7b00856.

[40] Z. Liu, G. Pang, S. Dong, Y. Zhang, C. Mi, X. Zhang, An aqueous rechargeable sodium−magnesium mixed ion battery based on $NaTi_2(PO_4)_3$–MnO_2 system, Electrochim. Acta 311 (2019) 1–7, https://doi.org/10.1016/j.electacta.2019.04.130.

[41] S. Chen, J. Wang, L. Fan, R. Ma, E. Zhang, Q. Liu, B. Lu, An ultrafast rechargeable hybrid sodium-based dual-ion capacitor based on hard carbon cathodes, Adv. Energy Mater. 8 (2018) 1800140, https://doi.org/10.1002/aenm.201800140.

[42] X. Guo, Z. Wang, W. Zhu, H. Yang, The novel and facile preparation of multilayer MoS2 crystals by a chelation-assisted sol-gel method and their electrochemical performance, RSC Adv. 7 (2017) 9009–9014, https://doi.org/10.1039/c6ra25558b.

[43] R. Thangavel, R. Ponraj, A.G. Kannan, K. Kaliyappan, D.W. Kim, Z. Chen, Y.S. Lee, High performance organic sodium-ion hybrid capacitors based on nano-structured disodium rhodizonate rivaling inorganic hybrid capacitors, Green Chem. 20 (2018) 4920–4931, https://doi.org/10.1039/c8gc01987h.

[44] R. Wang, S. Wang, X. Peng, Y. Zhang, D. Jin, P.K. Chu, L. Zhang, Elucidating the intercalation pseudocapacitance mechanism of MoS_2 -carbon monolayer interoverlapped superstructure: toward high-performance sodium-ion-based hybrid supercapacitor, ACS Appl. Mater. Interfaces 9 (2017) 32745–32755, https://doi.org/10.1021/acsami.7b09813.

[45] A. Müller, R. Jostes, W. Jaegermann, R. Bhattacharyya, Spectroscopic investigation on the molecular and electronic structure of $[Mo_3S_{13}]_2$-, a discrete binary transition metal sulfur cluster, Inorg. Chim. Acta. 41 (1980) 259–263, https://doi.org/10.1016/S0020-1693(00)88466-2.

[46] P. Scherrer, Bestimmung der Größe und der inneren Struktur von Kolloidteilchen mittels Röntgenstrahlen, Nachrichten von Der Gesellschaft Der Wissenschaften Zu Göttingen, Math. Klasse. 1918 (1918) 99–100.

[47] M.R. Gao, M.K.Y. Chan, Y. Sun, Edge-terminated molybdenum disulfide with a 9.4-Å interlayer spacing for electrochemical hydrogen production, Nat. Commun. 6 (2015) 1–8, https://doi.org/10.1038/ncomms8493.

[48] C. Zhan, W. Liu, M. Hu, Q. Liang, X. Yu, Y. Shen, R. Lv, F. Kang, Z.H. Huang, High-performance sodium-ion hybrid capacitors based on an interlayer-expanded MoS_2/rGO composite: surpassing the performance of lithium-ion capacitors in a uniform system, NPG Asia Mater. 10 (2018) 775–787, https://doi.org/10.1038/s41427-018-0073-y.

[49] NIST X-ray photoelectron spectroscopy (XPS) database, version 3.5, (n.d.). https://srdata.nist.gov/xps/. (Accessed 9 March 2021).

[50] L. Liang, V. Meunier, First-principles Raman spectra of MoS2, WS2 and their heterostructures, Nanoscale 6 (2014) 5394–5401, https://doi.org/10.1039/c3nr06906k.

[51] X. Zhang, X. Xu, W. He, G. Yang, J. Shen, J. Liu, Q. Liu, $LiFePO_4$/$NaFe_3V_9O_{19}$/porous glass nanocomposite cathodes for Li^+/Na^+ mixed-ion batteries, J. Mater. Chem. A. 3 (2015) 22247–22257, https://doi.org/10.1039/c5ta06424d.

[52] S.K. Park, J. Lee, , S. Bong, B. Jang, K.D. Seong, Y. Piao, Scalable synthesis of few-layer MoS_2 incorporated into hierarchical porous carbon nanosheets for high-performance Li- and Na-ion battery anodes, ACS Appl. Mater. Interfaces 8 (2016) 19456–19465, https://doi.org/10.1021/acsami.6b05010.

[53] H. Shu, F. Li, C. Hu, P. Liang, D. Cao, X. Chen, The capacity fading mechanism and improvement of cycling stability in MoS_2-based anode materials for lithium-ion batteries, Nanoscale 8 (2016) 2918–2926, https://doi.org/10.1039/c5nr07909h.

[54] X. Fan, D.J. Singh, W. Zheng, Valence band splitting on multilayer MoS_2: mixing of spin-orbit coupling and interlayer coupling, J. Phys. Chem. Lett. 7 (2016) 2175–2181, https://doi.org/10.1021/acs.jpclett.6b00693.

[55] J. Hao, J. Zheng, F. Ling, Y. Chen, H. Jing, T. Zhou, L. Fang, M. Zhou, Strain-engineered two-dimensional MoS_2 as anode material for performance enhancement of Li/Na-ion batteries, Sci. Rep. 8 (2018) 1–9, https://doi.org/10.1038/s41598-018-20334-z.

[56] G. Zhu, L. Ma, H. Lv, Y. Hu, T. Chen, R. Chen, J. Liang, X. Wang, Y. Wang, C. Yan, Z. Tie, Z. Jin, J. Liu, Pine needle-derived microporous nitrogen-doped carbon frameworks exhibit high performances in electrocatalytic hydrogen evolution reaction and supercapacitors, Nanoscale 9 (2017) 1237–1243, https://doi.org/10.1039/c6nr08139h.

[57] X. Wang, C. Zheng, L. Qi, H. Wang, Carbon derived from pine needles as a Na^+-storage electrode material in dual-ion batteries, Glob. Challenges. 1 (2017) 1700055, https://doi.org/10.1002/gch2.201700055.

[58] L. Chen, X. Cui, M. Wang, Y. Du, X. Zhang, G. Wan, L. Zhang, F. Cui, C. Wei, J. Shi, Microwave-Assisted synthesis of Co-coordinated hollow mesoporous carbon cubes for oxygen reduction reactions, Langmuir 31 (2015) 7644–7651, https://doi.org/10.1021/acs.langmuir.5b01256.

[59] Shindrov Kosova, Effect of mixed Li^+/Na^+-ion electrolyte on electrochemical performance of $Na_4Fe_3(PO_4)_2P_2O_7$ in hybrid batteries, Batteries 5 (2019) 39, https://doi.org/10.3390/batteries5020039.

[60] J. Wang, X. Zhang, W. He, Y. Yue, Y. Wang, C. Zhang, Layered hybrid phase $Li_2NaV_2(PO_4)_3$/carbon dot nanocomposite cathodes for Li^+/Na^+ mixed-ion batteries, RSC Adv. 7 (2017) 2658–2666, https://doi.org/10.1039/c6ra25808e.

[61] L. Chen, Q. Gu, X. Zhou, S. Lee, Y. Xia, Z. Liu, New-concept batteries based on aqueous Li^+/Na^+ mixed-ion electrolytes, Sci. Rep. 3 (2013) 1–7, https://doi.org/10.1038/srep01946.

[62] Q. Liu, H. Wang, C. Jiang, Y. Tang, Multi-ion strategies towards emerging rechargeable batteries with high performance, Energy Storage Mater (2019), https://doi.org/10.1016/j.ensm.2019.03.028.

[63] R. Wang, S. Wang, Y. Zhang, D. Jin, X. Tao, L. Zhang, Sodium storage in a promising MoS_2 -carbon anode: elucidating structural and interfacial transitions in the intercalation process and conversion reactions, Nanoscale 10 (2018) 11165–11175, https://doi.org/10.1039/c8nr02620c.

[64] C. Zhao, C. Yu, M. Zhang, Q. Sun, S. Li, M. Norouzi Banis, X. Han, Q. Dong, J. Yang, G. Wang, X. Sun, J. Qiu, Enhanced sodium storage capability enabled by super wide-interlayer-spacing MoS_2 integrated on carbon fibers, Nano Energy 41 (2017) 66–74, https://doi.org/10.1016/j.nanoen.2017.08.030.

[65] R. Wang, S. Wang, X. Peng, Y. Zhang, D. Jin, P.K. Chu, L. Zhang, Elucidating the intercalation pseudocapacitance mechanism of MoS_2-carbon monolayer interoverlapped superstructure: toward high-performance sodium-ion-based hybrid supercapacitor, ACS Appl. Mater. Interfaces 9 (2017), https://doi.org/10.1021/acsami.7b09813.

[66] C. Zhan, W. Liu, M. Hu, Q. Liang, X. Yu, Y. Shen, R. Lv, F. Kang, Z.H. Huang, High-performance sodium-ion hybrid capacitors based on an interlayer-expanded MoS_2/rGO composite: surpassing the performance of lithium-ion capacitors in a uniform system, NPG Asia Mater. 10 (2018), https://doi.org/10.1038/s41427-018-0073-y.

[67] H. Wang, D. Xu, G. Jia, Z. Mao, Y. Gong, B. He, R. Wang, H.J. Fan, Integration of flexibility, cyclability and high-capacity into one electrode for sodium-ion hybrid capacitors with low self-discharge rate, Energy Storage Mater 25 (2020) 114–123, https://doi.org/10.1016/j.ensm.2019.10.024.

[68] J. Liu, Y.G. Xu, L. Bin Kong, Synthesis of polyvalent ion reaction of MoS_2/CoS_2-RGO anode materials for high-performance sodium-ion batteries and sodium-ion capacitors, J. Colloid Interface Sci. 575 (2020) 42–53, https://doi.org/10.1016/j.jcis.2020.04.074.